

Satellite Dirac cones in phononic crystals

Received: 19 May 2025

Accepted: 26 November 2025

Published online: 18 December 2025

 Check for updatesHan Liu¹, Yuxiang Xi¹, Gangqiao Shao¹, Yinfei Zhang¹, Hailong He¹, Liping Ye¹, Manzhu Ke¹, Jiuyang Lu¹✉, Weiyin Deng¹✉ & Zhengyou Liu^{1,2}✉

Satellite Dirac cones in graphene systems are challenging to observe due to limited momentum-space resolution, hindering further exploration of their bulk-edge correspondence and associated transport properties. Here, we tackle this challenge by simplifying the bilayer configuration into a monolayer one with strong long-range couplings—an arrangement unattainable in natural materials but achievable in artificial structures for classical waves. Using phononic crystals for acoustic waves, we experimentally observe the satellite Dirac cones in the presence of third-nearest neighbor couplings and identify the acoustic edge states determined by their distinct non-trivial winding numbers. The satellite valleys emerge by introducing extra on-site potential, leading to multiple valley interface states. We further identify a frequency window enabling anomalous forward transport of the valley interface states in a standard four-channel splitter. Note that the introduction of long-range couplings is a systematic approach to engineering topological properties. Our findings establish a promising framework for multiple Dirac cones and valleys, opening new avenues for wave manipulation and signal processing in topological materials across both classical and quantum systems.

Following the rise of graphene, layer-stacked graphene came up to the stage as a platform for exploring a plethora of intriguing physics phenomena^{1–4}, such as unconventional quantum Hall effects^{5,6} and domain-wall valley transports^{7–9}. These phenomena are closely tied to the quadratic Dirac cone. It is demonstrated that, in the presence of trigonal warping effect, the quadratic Dirac cone is unstable and evolves into a central linear Dirac cone accompanied by three additional linear Dirac cones surrounding it, collectively referred to as satellite Dirac cones^{1,6,10–13}. Despite being proposed nearly two decades ago, satellite Dirac cones are experimentally challenging to identify, and their direct spectral observation remains elusive¹⁴.

Meanwhile, the Dirac cones inherently carry topological characteristics, as exemplified by the presence of edge states in graphene via the principle of bulk-edge correspondence^{15,16}. Additionally, introducing gaps in the Dirac cones leads to topological insulating phases, featuring by topologically protected edge or interfacial states¹⁷. Dirac cones and the associated topological transport are not confined to electronic systems and can be generalized to classical wave systems^{18–20}, where the flexibility in structural design allows the

relaxation of locality constraints in interactions. For example, roton-like dispersions can be driven by dominant long-range couplings in metamaterials^{21–25}, which enables the emergence of larger topological invariants^{26–30}. From this perspective, an intriguing question arises: could symmetry-permitted longer-ranged couplings generate additional Dirac cones in the Brillouin zone (BZ), forming satellite Dirac cones? If so, what would be the associated bulk-edge correspondence, and what novel phenomena might emerge if these satellite Dirac cones are gapped into satellite valleys?

In this work, we achieve the realization of satellite Dirac cones by introducing strong third-nearest-neighbor (TNN) couplings. These couplings enable the symmetry-protected Dirac cones in a monolayer honeycomb structure to generate satellite Dirac cones, accompanied by a band reshaping. The resulting satellite Dirac cones carry Berry phases in an opposite sign to that of the central cone. Consequently, satellite Dirac cones induce a doubling of edge states compared to the original one. Our model is implemented in phononic crystals (PCs), which have long served as versatile platforms for exploring topological phenomena^{19,20}. PCs offer flexibility for

¹Key Laboratory of Artificial Micro- and Nanostructures of Ministry of Education and School of Physics and Technology, Wuhan University, Wuhan, China.

²Institute for Advanced Studies, Wuhan University, Wuhan, China. ✉e-mail: jylu@whu.edu.cn; dengwy@whu.edu.cn; zyliu@whu.edu.cn

performing broadband measurements and facilitate counterintuitive couplings, including the strong TNN couplings required in this study. Moreover, by introducing staggered on-site potentials, the Dirac cones are gapped, forming satellite valleys that support multiple valley interfacial modes. The satellite Dirac cones and their associated transport phenomena are validated through both simulations and experiments. These findings highlight the potential of longer-range couplings in band engineering, enabling the emergence of topologically nontrivial phases.

Results

Lattice model with satellite Dirac cones

We incorporate TNN hoppings into a monolayer graphene lattice to achieve satellite Dirac cones, which significantly simplifies the scenario in Bernal-stacked bilayer graphene (see Supplementary Note 1). As illustrated in Fig. 1a, our model yields the following Bloch Hamiltonian in the (A, B) sublattice basis:

$$H(\mathbf{k}) = \begin{pmatrix} 0 & t_1\gamma_1(\mathbf{k}) + t_3\gamma_3(\mathbf{k}) \\ t_1\gamma_1^*(\mathbf{k}) + t_3\gamma_3^*(\mathbf{k}) & 0 \end{pmatrix}, \quad (1)$$

where t_1 and t_3 represent the nearest-neighbor and TNN hopping strengths, respectively, both of which are real-valued. The explicit forms of $\gamma_1(\mathbf{k})$ and $\gamma_3(\mathbf{k})$ are given as $\gamma_1 = 1 + e^{i\mathbf{k}\cdot\mathbf{a}_2} + e^{i\mathbf{k}\cdot(\mathbf{a}_2 - \mathbf{a}_1)}$ and $\gamma_3 = e^{-i\mathbf{k}\cdot\mathbf{a}_1} + e^{i\mathbf{k}\cdot\mathbf{a}_1} + e^{i\mathbf{k}\cdot(2\mathbf{a}_2 - \mathbf{a}_1)}$, with primitive lattice vectors defined as $\mathbf{a}_1 = (1, 0)$ and $\mathbf{a}_2 = (1/2, \sqrt{3}/2)$. The eigenvalues of $H(\mathbf{k})$ are given by $E_{\pm} = \pm |t_1\gamma_1(\mathbf{k}) + t_3\gamma_3(\mathbf{k})|$, and the band-touching points are determined by solving $E_{\pm} = 0$. The existence of these solutions is guaranteed by the combined symmetries of time-reversal and spatial inversion. In real graphene, the TNN hopping strength (t_3) is approximately 40 times

weaker than t_1 ¹, and thus t_3 is often neglected when analyzing electronic properties of graphene. This approximation gives rise to the well-known Dirac cones at the corners of the BZ.

To explore the impact of stronger beyond-neighbor couplings ($t_3 > t_1$), we show the evolution of the Dirac points as t_3 increases, as depicted in Fig. 1b. Notably, this evolution induced by TNN hoppings resembles a Lifshitz transition in non-interacting systems³¹, and, in twist-bilayer graphene near magic angle, similar Dirac cone evolution and Berry curvature distributions can be observed³². Starting from $t_3 = 0$, where a regular Dirac cone is located at K , increasing t_3 gradually reduces the gap at M until it closes at $t_3 = t_1/3$. This gap closure corresponds to the formation of a semi-Dirac cone characterized by an anisotropic Fermi velocity. As t_3 continues to increase, the semi-Dirac cone splits into two Dirac cones along $K-K'$. Subsequently, when $t_3 = t_1/2$, these Dirac cones merge with the central cone at K , resulting in a quadratic node, which accounts for the low-energy band structure in Bernal-stacked bilayer graphene without trigonal warping. Further increasing t_3 , the satellite Dirac cones reappear from the quadratic band crossing along the ΓK directions, resembling the trigonal warping effect. A summary of these Dirac cones with their low-energy Hamiltonians is provided in Supplementary Note 2 with Table S1. Hereafter, we concentrate on the regime of stronger t_3 , using $t_3 = 3t_1$ as a representative case.

We investigate the topological property and bulk-edge correspondence associated with the satellite Dirac cones. The eigenstates of Hamiltonian in Eq. (1) take a spinor form, $|u_{\pm}(\mathbf{k})\rangle = 1/\sqrt{2}(\pm 1, e^{i\theta(\mathbf{k})})^T$, where θ represents the phase difference between the two sublattices. This phase accumulates over a closed loop around the Dirac cone and yields its Berry phase. Figure 1c shows the distribution of $\theta(\mathbf{k})$ in reciprocal space. At each corner of the BZ, there exists a central Dirac

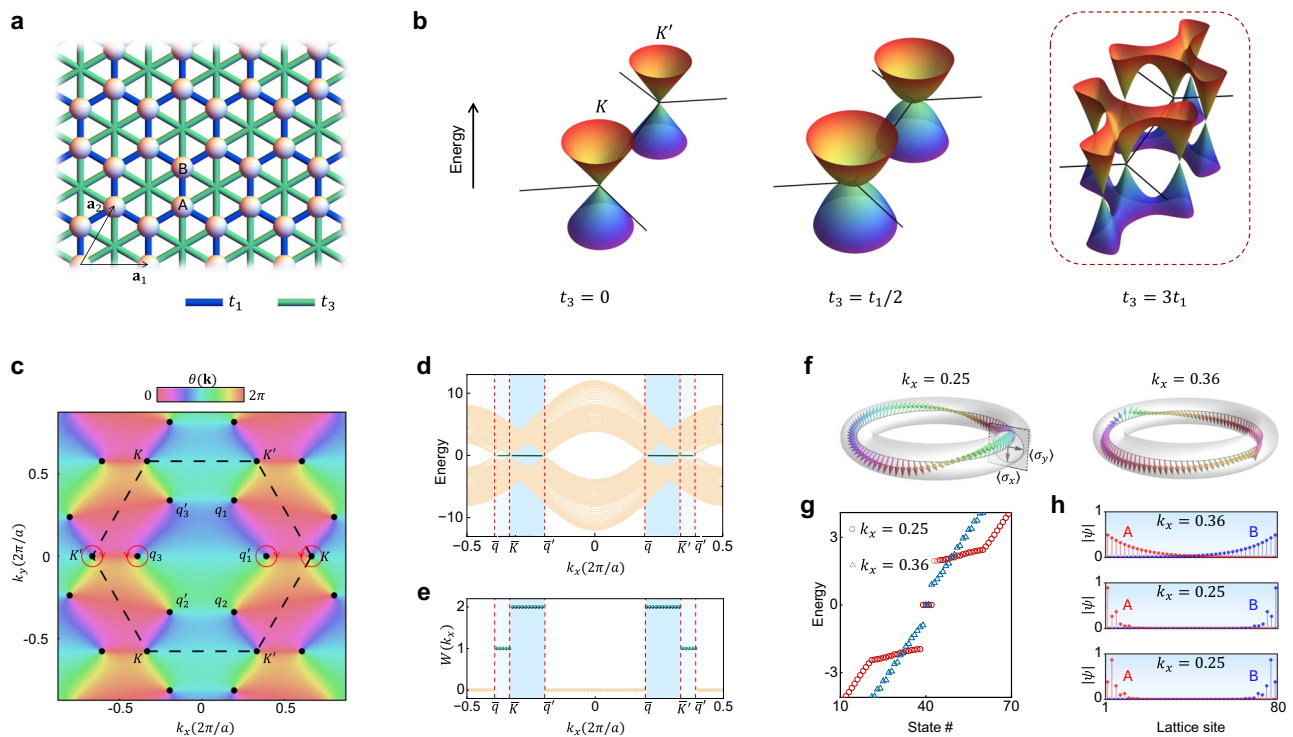


Fig. 1 | Lattice model and bulk-edge correspondence for satellite Dirac cones. **a** Schematic of the graphene lattice with nearest-neighbor couplings t_1 and TNN couplings t_3 . **b** Evolution of the band structure as t_3 increases. The red dashed box highlights the appearance of satellite Dirac cones with $t_3 = 3t_1$. **c** Distribution of Dirac nodes (black dots) in reciprocal space, with the colormap denoting θ . The dashed hexagon indicates the first BZ. **d, e** Projected band spectrum and the

corresponding winding numbers along k_x , respectively. **f** Evolution of single-band pseudospins $\hat{\mathbf{n}}$ over a periodic cycle in k_y (toroidal direction). The left panel corresponds to $k_x = 0.25$ with the winding number $W = 2$, while the right panel corresponds to $k_x = 0.36$ with $W = 1$. **g** Eigen spectra for $k_x = 0.25$ and 0.36 , obtained using a strip geometry with 40 unit cells. **h** Distributions of the corresponding zero-energy edge states.

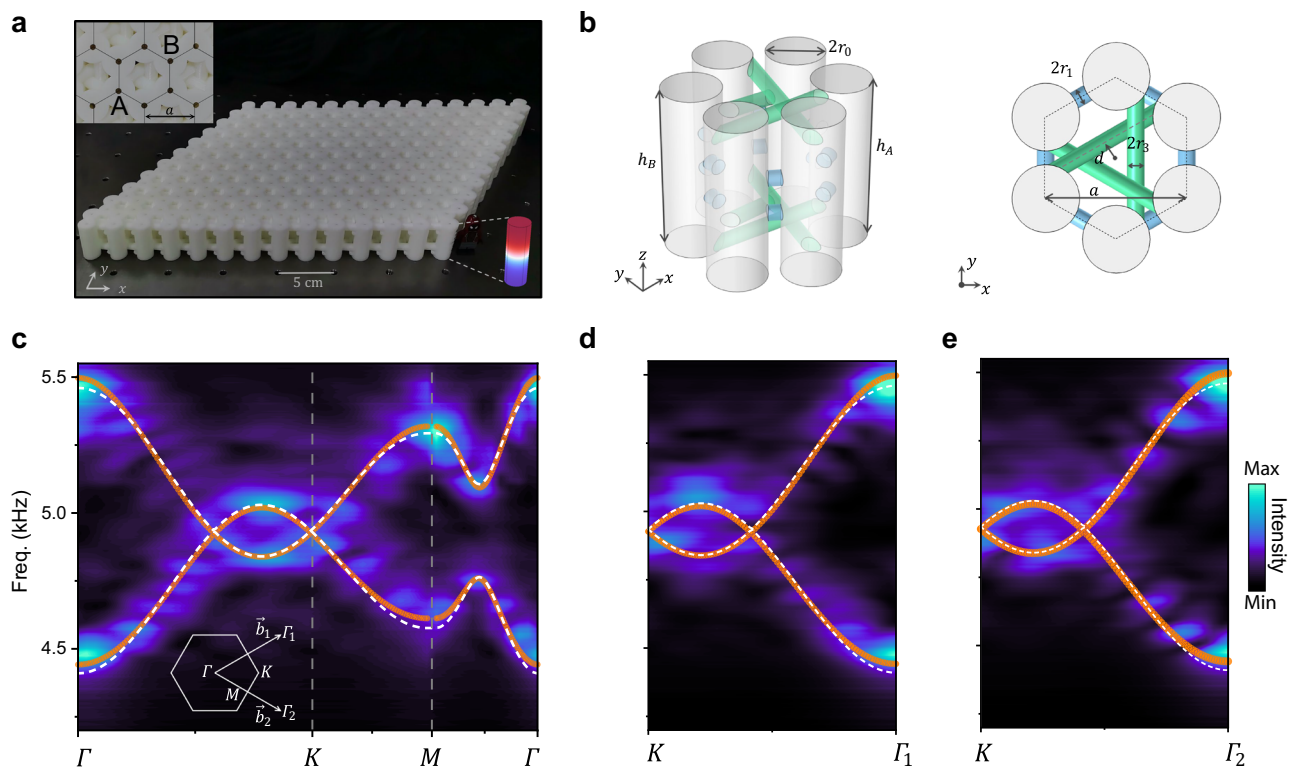


Fig. 2 | Probing acoustic satellite Dirac cones. **a** Photograph of the PC. The upper inset shows a zoomed-in view of the structure, while the lower inset illustrates the first longitudinal cavity mode. **b** Schematic of the PC design to achieve strong TNN couplings. The labeled parameters are $h_0 = 35$ mm, $r_0 = 6$ mm, $r_1 = r_3 = 1.55$ mm and

$d = 3.46$ mm. The dashed hexagon labels a unit cell. **c** Acoustic dispersions obtained from experiments (colormaps), simulations (orange curves) and the tight-binding model (white dashed lines), respectively. The inset denotes the schematic for BZ. **d, e** Measured acoustic dispersions (colormaps) along $K\Gamma_1$ and $K\Gamma_2$, respectively.

cone, acting as a phase singularity for $\theta(\mathbf{k})$. Due to the presence of strong TNN couplings, three satellite Dirac cones appear and are trigonally wrapped around the central one with reversed phase vorticity, resulting in a total of eight Dirac cones in the first BZ.

Figure 1d shows the spectra in projected 1D BZ for a ribbon with bearded edges, with spectral color denotes state localization. Localized zero-energy edge states are found threading the projections of Dirac cones in blue-shaded regions. The appearance of these edge states corresponds to the nontrivial values of the winding number $W(k_x) = (2\pi i)^{-1} \oint dk_y \partial_{k_y} [\log(t_1 \gamma_1 + t_3 \gamma_3)]$, as shown in Fig. 1e. Beyond $W = 1$ regions, higher $W = 2$ regions are clearly observed, which originates from a twice change in phase induced by additional satellite Dirac cones. The winding number can also be intuitively viewed by counting the winding number of pseudospin vector as k_y traverses the BZ. Under a proper gauge choice, one can define a pseudospin vector $\hat{\mathbf{n}}(\mathbf{k}) \equiv (\langle \sigma_y \rangle, -\langle \sigma_x \rangle)$ and track its evolution, where $\langle \sigma_s \rangle$ represents the expectation value of the Pauli matrices for the eigenstate $|u_+(\mathbf{k})\rangle$. For example, as shown in Fig. 1f, at $k_x = 0.25$, the pseudospin vector completes two full twists before returning to its starting point, indicating $W = 2$. In contrast, at $k_x = 0.36$, the pseudospin vector exhibits a single twist, corresponding to $W = 1$. For k_x with trivial W values, the pseudospin vector shows no winding at all. Consequently, a doubled number of edge states occur at $k_x = 0.25$ in Fig. 1g, compared to a single pair at $k_x = 0.36$. We further visualize the distributions of these edge states in Fig. 1h, where edge states with larger winding numbers exhibit shorter decay lengths. By extending the coupling range, additional Dirac points and higher winding numbers become attainable, as summarized in Table S2 of Supplementary Note 8, highlighting that long-range couplings provide a simple and systematic approach for

engineering topological band degeneracies and manipulating topological invariants^{33,34}.

Acoustic Realizations

To realize satellite Dirac points experimentally, we design an acoustic analog of graphene with enhanced TNN couplings. Figure 2a presents a photograph of our 3D-printed sample, where cylindrical cavities are connected by pipe to form a honeycomb structure with 14×11 unit cells in the x - y plane, with a lattice constant of $a = 25$ mm. Figure 2b shows the schematic of the sample design for realizing stronger acoustic TNN couplings (see Supplementary Note 3 with Fig. S3 for geometric details). All cavities in the structure are identical in height and diameter, ensuring that the unit cell belongs to the point group D_3 , which guarantees the band crossings at BZ corners of PC. In the experiment, the system is driven near the frequency of the first longitudinal cavity mode, which features a wave node at the midplane of the cavity (lower-right inset in Fig. 2a). This mode strengthens the coupling for tubes connected at the cavity ends, while reducing the coupling for tubes connected near the midplane. This design facilitates the required TNN couplings for achieving the acoustic satellite Dirac points.

The measured bulk dispersion is depicted in Fig. 2c, which matches well with the simulated and analytical results represented by orange solid and white dashed lines. These results confirm the appearance of extra Dirac cone dispersions along the Γ - K line, arising from the interplay between strong TNN couplings and trigonal crystalline symmetry. Figure 2d, e present the measured acoustic dispersions along $K\Gamma_1$ and $K\Gamma_2$, further confirming the presence of satellite structure in band crossings around frequency $f_D = 4.94$ kHz. The

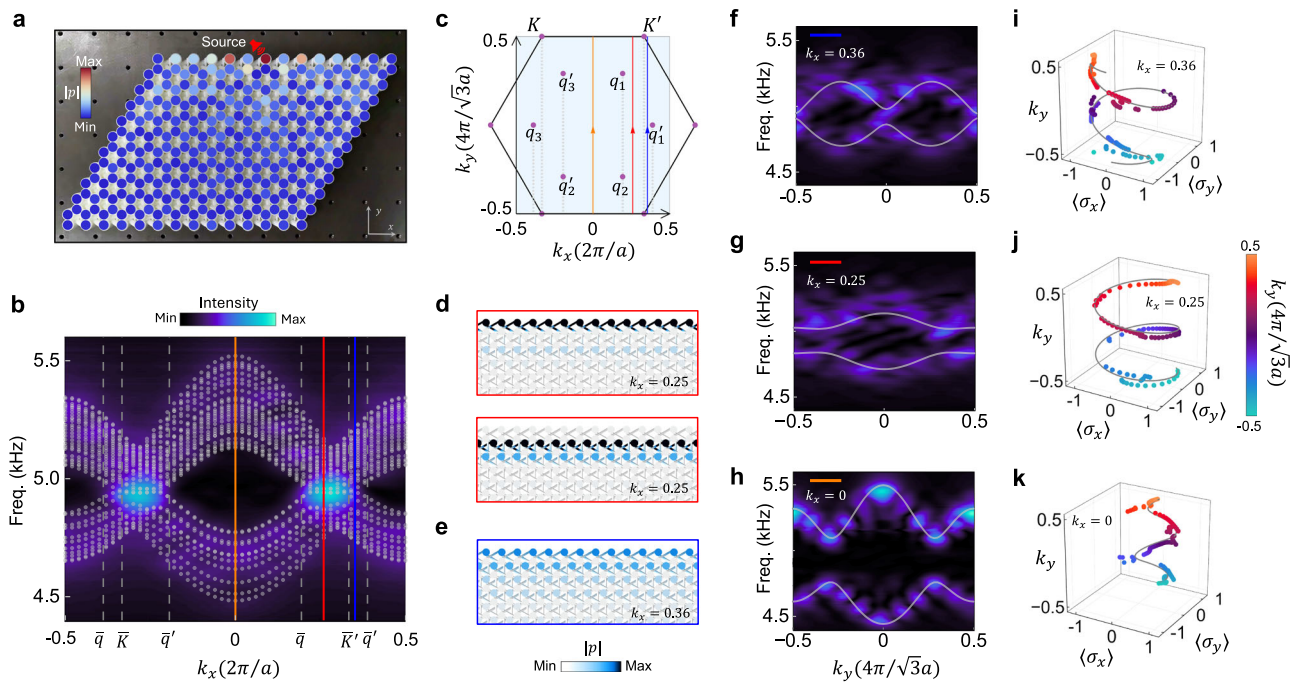


Fig. 3 | Experimental validation of edge states and bulk-edge correspondence for acoustic satellite Dirac cones. **a** Measured acoustic pressure field of the PC with a source placed at the middle of the upper boundary. **b** Measured (colormaps) and simulated (gray dots) acoustic edge state dispersions. **c** Schematic of the first BZ. The vertical dashed lines in (**b**) mark the projections of Dirac points, as

illustrated in (**c**), while the vertical solid lines in orange, red, and blue highlight $k_x = 0, 0.25$, and 0.36 , respectively. **d, e** Simulated acoustic eigenfields at the upper boundary for $k_x = 0.25$ and 0.36 , respectively. **f–h** Acoustic bulk dispersions along the colored vertical lines in (**c**). **i–k** Measured (dots) and simulated (lines) pseudospin trajectories of the first bands in (**f–h**).

measured frequency contours near K and K' are present in Supplementary Fig. S4. Note that the absence of genuine chiral symmetry in the real system leads to slightly different dispersions above and below f_D . Nevertheless, our PC captures the key features and profiles of the satellite Dirac cones with high fidelity. One can further improve the resolution of measured dispersions by using samples with more unit cells.

We further experimentally validate the bulk-edge correspondence in the gapless PC with satellite Dirac cones. Excited by a point-source placed in an edge cavity of the PC, the scanned acoustic pressure field is displayed in Fig. 3a. The measured field decays more rapidly toward the bulk than along the edge, indicating the existence of edge states. The response spectra of the sample in edge and bulk area are given in Fig. S5. Figure 3b shows the projected dispersion as a function of k_x , where the colormaps represent experimental results and the dots correspond to simulated dispersions for a strip with bearded edges. Around the Dirac frequency f_D , the bright colormaps align with the simulated edge states along k_x , covering the wavevectors between satellite Dirac point projections, as illustrated in Fig. 3c. Specifically, at $k_x = 0.25$, four edge modes are present, with the simulated acoustic pressure fields shown in Fig. 3d (only the upper boundary is displayed for clarity). Similarly, at $k_x = 0.36$, two edge modes are observed with the corresponding fields shown in Fig. 3e. Simulated results for acoustic edge states with zigzag boundaries are provided in Supplementary Fig. S6. These simulated and experimental results show good agreement, providing support for the satellite Dirac points in our acoustic system.

In experiments, the response signal near the sample boundary generally results from a collective contribution of all edge modes. This complicates a clear experimental identification of the k_x -dependent bulk-edge correspondence solely based on edge responses, as shown in Fig. 3b. To address this subtlety, we measure the variation of pseudospin ($\langle \sigma_x \rangle, \langle \sigma_y \rangle$) across a k_y path at three specific k_x , marked by

colored solid lines in Fig. 3c, which provides an intuitive representation of the winding numbers that corresponds to the number of edge states, as discussed in the lattice model. Figure 3f–h shows the gapped bulk dispersions along k_y at three representative k_x values, which can alternatively be interpreted as the dispersions of reduced 1D subsystems parameterized by different k_x . For each subsystem, the spinor used to construct $\langle \sigma_i \rangle$ is approximated by Fourier transforming the response of a single band from the two sublattices separately (see Methods and Supplementary Note 4 with Fig. S7). The corresponding pseudospin trajectories for the first band over a k_y -cycle are depicted in Fig. 3i–k. In Fig. 3i, the pseudospin winds around the origin once, corresponding to the presence of the two edge states at $k_x = 0.36$. At $k_x = 0.25$, where four edge states are present, a double winding of the pseudospin spiral is clearly observed in Fig. 3j. Finally, at $k_x = 0$, the pseudospin trajectory oscillates back and forth without forming a winding, as illustrated in Fig. 3k, which accounts for the absence of edge state responses. To show the extensibility of our approach, we further experimentally identified a winding number of 3 in a similar honeycomb PC with strong eighth-nearest-neighbor couplings (see Supplementary Note 8), further confirming that longer-range couplings enable larger winding numbers.

The satellite-valley interface states

We further explore the acoustic valley interface states related to the satellite Dirac cones. A typical sample with a zigzag-type interface is shown in Fig. 4a. The staggered sublattice potential is introduced by varying the cavity heights, $h_B - h_A = \pm \delta$ with $\delta = 0.05h_0$ for the two distinct phases I and II. As such, the satellite Dirac cones split into satellite valleys located around $K(K')$ with opposite Berry curvatures, resulting in multi-valley insulating phases, as shown in Fig. 4b. Consequently, as shown in Fig. 4c, the valley interface channel holds four guiding modes, each exhibiting two valley polarizations propagating in the same direction (see Supplementary Note 9 for the lattice model

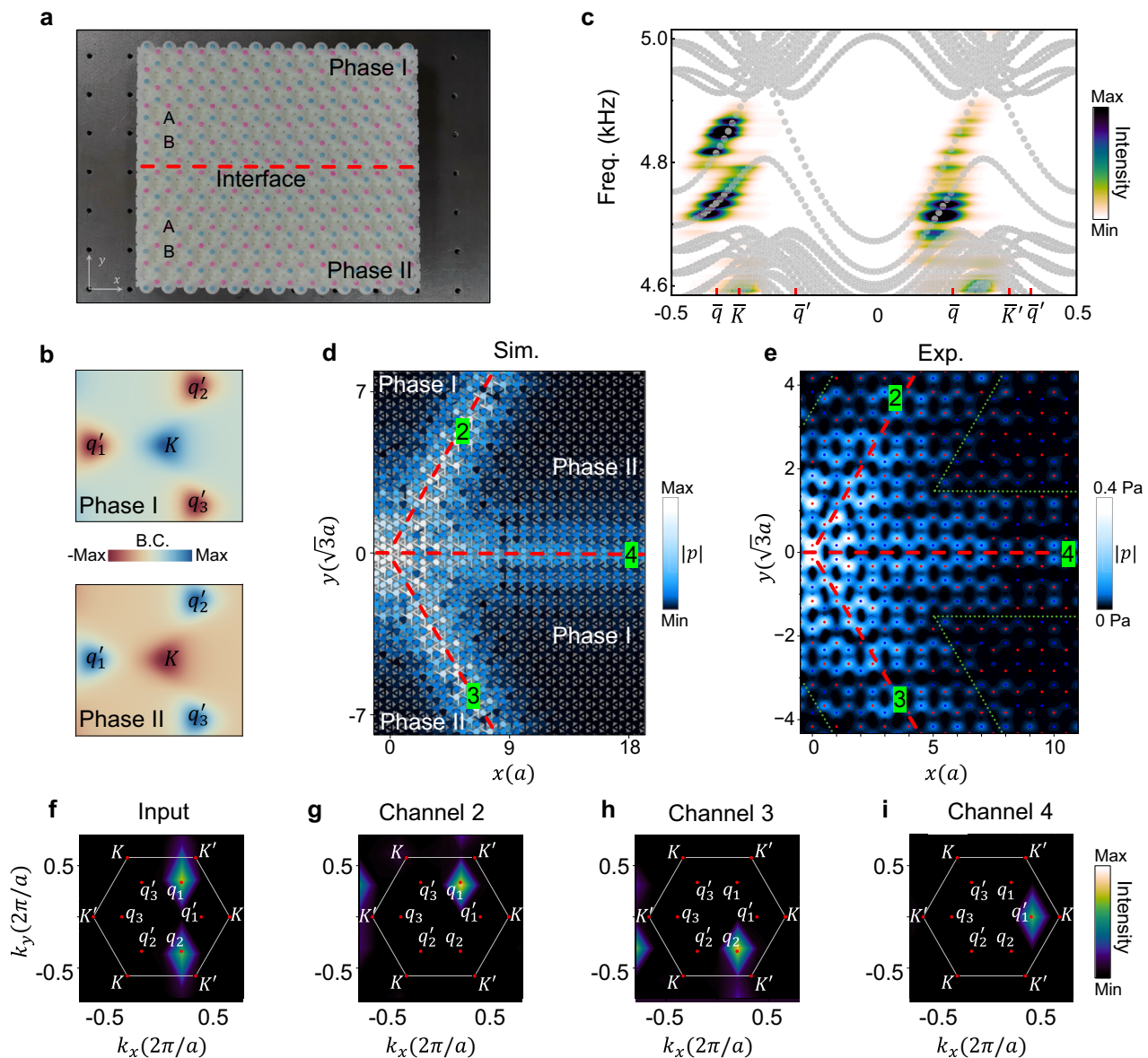


Fig. 4 | Experimental demonstration of satellite-valley interface states.

a Photograph of the sample, consisting of two phases with different on-site biases δ . The red dashed line denotes the interface. **b** Simulated Berry curvature distribution around K for the two phases. **c** Measured (colormaps) and simulated (dots) dispersions of guiding modes along the interface shown in (a). **d, e** Simulated and experimentally measured acoustic pressure field splitting. The red dashed lines

denote the interfaces, and the numbers indicate the three output channels. The green dotted lines in (e) outline the region of the interface states, and the red and blue points further highlight the cavities with different δ . **f–i** Measured Fourier spectra of the acoustic field for the four channels, with the red dots indicating the positions of valleys.

results). Distinct from approaches rely on high-order modes³⁵, these interface states arise from satellite valleys induced by long-range couplings, enabling a wider frequency window. The robustness of these valley guiding modes against sharp path bends is demonstrated in Supplementary Note 9.

As is well known, the preservation of valley pseudospin enables valley-locked one-way topological transport, which plays a key role in governing wave behavior in a prototypical four-channel beam splitter. These splitters serve as fundamental building block for functional topological valley-based networks. Note that in the multi-valley cases, the Berry curvature becomes more diffuse, facilitating inter-valley transitions. We exploit these transitions to enable transmission through channels otherwise forbidden by valley locking. As illustrated in Fig. 4d, we construct such a beam splitter by combining

two distinct phases (see Supplementary Note 5 with Figs. S8 and S9 for the configuration details of the splitter and eigenfields in the channels), with the input channel as shown in Fig. 4a. We then stimulate the acoustic interface state carrying valley index q at the input channel and examine how it bifurcates at the intersection. Remarkably, within a frequency window of approximately 4.73–4.78 kHz, the acoustic interface state can transport forward into channel 4, as demonstrated by both simulations and experiments shown in Fig. 4d, e. Note that such forward transport is previously heavily suppressed due to the mismatched valley polarization, while here the satellite valleys enable this anomalous forward transport. Outside this frequency window, the system exhibits normal wave-splitting behavior (see Supplementary Note 6 for the channel transmissions at different frequencies). The measured Fourier spectra at 4.75 kHz for the

channels are presented in Fig. 4f–i. For a q -valley polarized input acoustic wave, the output waves from channels 2 and 3 retain the valley polarization as expected (Fig. 4g, h). However, the acoustic wave in channel 4 is converted to be q' -valley polarized (Fig. 4i), breaking the valley conservation. This is probably caused by inter-valley scattering, which occurs due to reduced momentum-space separation between the valleys³⁶. (see Supplementary Note 7 with Fig. S13 for simulated results of the splitter with different interface configurations). This phenomenon may add fresh ingredients for valleytronics and valley-based transportation.

Discussion

In conclusion, we have demonstrated the satellite Dirac cones induced by strong TNN couplings. The acoustic satellite Dirac cones are directly observed in PCs through bulk dispersion measurements, and crucially, their wavevector-dependent nontrivial topology is experimentally determined for the first time, providing a valuable supplement to methods of measuring topological invariants^{37,38}. According to bulk-edge correspondence, the satellite Dirac cones bring about a doubling of zero edge states. Moreover, TNN coupling enhanced multi-valley transport is observed by introducing staggered on-site potentials, enabling the formation of an acoustic splitter with anomalous forward propagation^{39–46}, which offers a promising approach for realizing valley inverters^{47–49}. Our findings introduce an easy-to-implement mechanism for engineering topological properties, adding fresh avenues for exploring novel topological phases and inspiring further research on beyond-nearest-neighbor couplings in metamaterials^{50,51}. This design could be further scaled down to the on-chip level^{22,42}, with significant potential for robust information telecommunications and particle manipulations^{44,52,53}.

Methods

Experiments

The PC samples were fabricated by 3D printing, using photosensitive resin. The wall thickness of all cavities and connecting tubes was set at 2 mm. Due to the significant impedance mismatch, the walls act as rigid boundaries for sound waves. Small holes (3 mm in diameter) were drilled on top of each cavity to facilitate the excitation and probing of sound signals; these holes were sealed with stoppers when not in use. In experiments, a network analyzer (B&K Type 3560B) was employed to generate and analyze the signals in the frequency domain, with a frequency step of 4 Hz. Sound generation was achieved using loudspeakers (about 2 mm in diameter) inserted into designed cavities, while sound detection was carried out using two acoustic probes. One probe (B&K Type 4187 1/4-inch microphone) was fixed near the sound source to collect the reference signals, while the other (B&K Type 4182) was manually swept in the sampling area of desired cavities to measure the field distributions (Fig. 4e). Spatial Fourier transformations of the acoustic fields were performed to extract the corresponding dispersions for bulk states (Fig. 2c–e), edge states (Fig. 3b), and interface states (Fig. 4c and Fig. 4f–i).

The experimental method for extracting pseudospin windings in Fig. 3i–k is detailed as follows. A point source was placed in a bulk cavity of the sample shown in Fig. 2a to generate sound waves (see Supplementary Fig. S5 for the measured response spectrum). The acoustic fields in sublattice cavities A and B were separately recorded and subjected to Fourier transformations. From the transformed data, the one-dimensional bulk band versus k_y was extracted at $k_x = k_{xi}$ as shown in Fig. 3f–h. The response intensity of a single band at wavevector k_{yi} and frequency f_i was approximated by a peak, which was subsequently Fourier transformed to yield extended waves in real space y . Using the transformed data, the field amplitudes at the same y from the two sublattices were adopted to construct the spinors, thereby obtaining the pseudospin vector at k_{yi} . This procedure is described in Supplementary Note 4 with Fig. S7. This process was

repeated for each k_{yi} and yielded the pseudospin windings shown in Fig. 3i–k.

Simulations

All simulations of PCs were implemented with COMSOL Multiphysics, a finite element solver package. The speed of sound in air was set to 344 m/s at room temperature and the air density was 1.29 kg/m³. The solid walls of the sample were treated as rigid boundaries. To obtain the bulk dispersions (orange line in Fig. 2c), periodic boundary conditions were applied to the unit cell in both directions. For the projected bands corresponding to edge states (dotted lines in Fig. 3b), a strip-like supercell consisting of 11 unit cells along the y direction was used, with solid boundary conditions on the edges and periodic boundary conditions along the x direction. The calculation of valley interface states in Fig. 4c was carried out in a similar way, with states localized at the external edges filtered out for clarity. To simulate the frequency-domain field distributions shown in Fig. 4d, two identical point sources were placed in two interface cavities at $x = -10$. Sound damping in simulation was incorporated by assigning an imaginary part of the sound velocity with a value of 0.5im/s. The height of the point sources was set to $0.9(h_A - \delta)$ for exciting the acoustic field.

Data availability

The data that support the plots within this paper and other findings of this study are available from the corresponding author upon request.

Code availability

The codes that support the results of this study are available from the corresponding authors upon request.

References

- McCann, E. & Koshino, M. The electronic properties of bilayer graphene. *Rep. Prog. Phys.* **76**, 056503 (2013).
- Bernevig, B. A. & Efetov, D. K. Twisted bilayer graphene's gallery of phases. *Phys. Today* **77**, 38 (2024).
- Cao, Y. et al. Unconventional superconductivity in magic-angle graphene superlattices. *Nature* **556**, 43 (2018).
- Zhang, F., Jung, J., Fiete, G. A., Niu, Q. & MacDonald, A. H. Spontaneous quantum Hall states in chirally stacked few-layer graphene systems. *Phys. Rev. Lett.* **106**, 156801 (2011).
- Novoselov, K. S. et al. Unconventional quantum Hall effect and Berry's phase of 2π in bilayer graphene. *Nat. Phys.* **2**, 177 (2006).
- McCann, E. & Fal'ko, V. I. Landau-level degeneracy and quantum Hall effect in a graphite bilayer. *Phys. Rev. Lett.* **96**, 086805 (2006).
- Zhang, F., MacDonald, A. H. & Mele, E. J. Valley Chern numbers and boundary modes in gapped bilayer graphene. *Proc. Natl. Acad. Sci. USA* **110**, 10546 (2013).
- Ju, L. et al. Topological valley transport at bilayer graphene domain walls. *Nature* **520**, 650 (2015).
- Li, J. et al. Gate-controlled topological conducting channels in bilayer graphene. *Nat. Nanotechnol.* **11**, 1060 (2016).
- Koshino, M. & Ando, T. Transport in bilayer graphene: calculations within a self-consistent Born approximation. *Phys. Rev. B* **73**, 245403 (2006).
- Mikitik, G. P. & Sharlai, Y. u.V. Electron energy spectrum and the Berry phase in a graphite bilayer. *Phys. Rev. B* **77**, 113407 (2008).
- Sun, K., Yao, H., Fradkin, E. & Kivelson, S. A. Topological insulators and nematic phases from spontaneous symmetry breaking in 2D fermi systems with a quadratic band crossing. *Phys. Rev. Lett.* **103**, 046811 (2009).
- de Gail, R., Goerbig, M. O. & Montambaux, G. Magnetic spectrum of trigonally warped bilayer graphene: Semiclassical analysis, zero modes, and topological winding numbers. *Phys. Rev. B* **86**, 045407 (2012).

14. Seiler, A. M. et al. Probing the tunable multi-cone band structure in Bernal bilayer graphene. *Nat. Commun.* **15**, 3133 (2024).
15. Ryu, S. & Hatsugai, Y. Topological origin of zero-energy edge states in particle-hole symmetric systems. *Phys. Rev. Lett.* **89**, 077002 (2002).
16. Delplace, P., Ullmo, D. & Montambaux, G. Zak phase and the existence of edge states in graphene. *Phys. Rev. B* **84**, 195452 (2011).
17. Qi, X.-L. & Zhang, S.-C. Topological insulators and superconductors. *Rev. Mod. Phys.* **83**, 1057 (2011).
18. Ozawa, T. et al. Topological photonics. *Rev. Mod. Phys.* **91**, 015006 (2019).
19. Zhang, X., Zangeneh-Nejad, F., Chen, Z.-G., Lu, M.-H. & Christensen, J. A second wave of topological phenomena in photonics and acoustics. *Nature* **618**, 687 (2023).
20. Shah, T., Brendel, C., Peano, V. & Marquardt, F. *Colloquium: topologically protected transport in engineered mechanical systems.* *Rev. Mod. Phys.* **96**, 021002 (2024).
21. Chen, Y., Kadic, M. & Wegener, M. Roton-like acoustical dispersion relations in 3D metamaterials. *Nat. Commun.* **12**, 3278 (2021).
22. Martínez, J. A. I. et al. Experimental observation of roton-like dispersion relations in metamaterials. *Sci. Adv.* **7**, eabm2189 (2021).
23. Zhu, Z. et al. Observation of multiple rotons and multidirectional roton-like dispersion relations in acoustic metamaterials. *New J. Phys.* **24**, 123019 (2022).
24. Bossart, A. & Fleury, R. Extreme spatial dispersion in nonlocally resonant elastic metamaterials. *Phys. Rev. Lett.* **130**, 207201 (2023).
25. Kazemi, A. et al. Drawing dispersion curves: band structure customization via nonlocal phononic crystals. *Phys. Rev. Lett.* **131**, 176101 (2023).
26. Lin, L., Ke, Y. & Lee, C. Real-space representation of the winding number for a one-dimensional chiral-symmetric topological insulator. *Phys. Rev. B* **103**, 224208 (2021).
27. Benalcazar, W. A. & Cerjan, A. Chiral-symmetric higher-order topological phases of matter. *Phys. Rev. Lett.* **128**, 127601 (2022).
28. Wang, D. et al. Realization of a Z-classified chiral-symmetric higher-order topological insulator in a coupling-inverted acoustic crystal. *Phys. Rev. Lett.* **131**, 157201 (2023).
29. Li, Y., Qiu, H., Zhang, Q. & Qiu, C. Acoustic higher-order topological insulators protected by multipole chiral numbers. *Phys. Rev. B* **108**, 205135 (2023).
30. Liu, H. et al. Acoustic topological metamaterials of large winding number. *Phys. Rev. Appl.* **19**, 054028 (2023).
31. Volovik, G. E. Exotic Lifshitz transitions in topological materials. *Phys. Usp.* **61**, 89 (2018).
32. Cao, Y. et al. Correlated insulator behaviour at half-filling in magic-angle graphene superlattices. *Nature* **556**, 80 (2018).
33. Ahn, S. J. et al. Dirac electrons in a dodecagonal graphene quasicrystal. *Science* **361**, 782 (2018).
34. Liang, Y., Zhan, J., Xia, S., Song, D. & Chen, Z. Observation of doubly degenerate topological flatbands of edge states in strained graphene. *Adv. Photonics* **7**, 046005 (2025).
35. Yan, B. et al. Multifrequency and multimode topological waveguides in a stampfli-triangle photonic crystal with large valley Chern numbers. *Laser Photon. Rev.* **18**, 2300686 (2024).
36. Xiao, D., Yao, W. & Niu, Q. Valley-contrasting physics in graphene: magnetic moment and topological transport. *Phys. Rev. Lett.* **99**, 236809 (2007).
37. Lin, Z.-K. et al. Measuring entanglement entropy and its topological signature for phononic systems. *Nat. Commun.* **15**, 1601 (2024).
38. Chen, Z.-X. et al. Direct measurement of topological invariants through temporal adiabatic evolution of bulk states in the synthetic Brillouin zone. *Phys. Rev. Lett.* **134**, 136601 (2025).
39. Qiao, Z., Jung, J., Niu, Q. & MacDonald, A. H. Electronic highways in bilayer graphene. *Nano Lett.* **11**, 3453 (2011).
40. Qiao, Z. et al. Current partition at topological channel intersections. *Phys. Rev. Lett.* **112**, 206601 (2014).
41. Lu, J. et al. Observation of topological valley transport of sound in sonic crystals. *Nat. Phys.* **13**, 369 (2017).
42. Yan, M. et al. On-chip valley topological materials for elastic wave manipulation. *Nat. Mater.* **17**, 993 (2018).
43. Zhang, Q. et al. Gigahertz topological valley Hall effect in nanoelectromechanical phononic crystals. *Nat. Electron.* **5**, 157 (2022).
44. Wang, W. et al. On-chip topological beamformer for multi-link terahertz 6G to XG wireless. *Nature (London)* **632**, 522 (2024).
45. Liu, J.-W. et al. Valley photonic crystals. *Adv. Phys.: X* **6**, 1905546 (2021).
46. Xue, H., Yang, Y. & Zhang, B. Topological valley photonics: physics and device applications. *Adv. Photonics Res.* **2**, 2100013 (2021).
47. Rycerz, A., Tworzydło, J. & Beenakker, C. W. J. Valley filter and valley valve in graphene. *Nat. Phys.* **3**, 172 (2007).
48. Wang, M. et al. Observation of boundary induced chiral anomaly bulk states and their transport properties. *Nat. Commun.* **13**, 5916 (2022).
49. Wu, H. et al. Acoustic valley filter, valve, and diverter. *Adv. Mater.* **37**, 2500757 (2025).
50. Chen, Y. et al. Anomalous frozen evanescent phonons. *Nat. Commun.* **15**, 8882 (2024).
51. Pellerin, F., Houvenaghel, R., Coish, W. A., Carusotto, I. & St-Jean, P. Wave-function tomography of topological dimer chains with long-range couplings. *Phys. Rev. Lett.* **132**, 183802 (2024).
52. Yang, Y. et al. Terahertz topological photonics for on-chip communication. *Nat. Photonics* **14**, 446 (2020).
53. Zhao, S. et al. Topological acoustofluidics. *Nat. Mater.* **24**, 707 (2025).

Acknowledgements

This work is supported by the National Key R&D Program of China (Nos. 2022YFA1404500, 2022YFA1404900), National Natural Science Foundation of China (Nos. 12222405, 12374419, 12374409, 12574024, and 12574484).

Author contributions

J.L., W.D., and Z.L. conceived the original idea. H.L., J.L., G.S., Y.Z., and H.H. did theoretical analysis and designed the structures. H.L., Y.X., L.Y., and M.K. performed the experiments. H.L., J.L., W.D., and Z.L. analyzed the data and wrote the manuscript. Z.L. supervised the project. All authors participated in discussions and reviewed the paper.

Competing interests

The authors declare no competing interests.

Additional information

Supplementary information The online version contains supplementary material available at <https://doi.org/10.1038/s41467-025-67305-3>.

Correspondence and requests for materials should be addressed to Jiuyang Lu, Weiyin Deng or Zhengyou Liu.

Peer review information *Nature Communications* thanks the anonymous reviewer(s) for their contribution to the peer review of this work. A peer review file is available.

Reprints and permissions information is available at <http://www.nature.com/reprints>

Publisher's note Springer Nature remains neutral with regard to jurisdictional claims in published maps and institutional affiliations.

Open Access This article is licensed under a Creative Commons Attribution-NonCommercial-NoDerivatives 4.0 International License, which permits any non-commercial use, sharing, distribution and reproduction in any medium or format, as long as you give appropriate credit to the original author(s) and the source, provide a link to the Creative Commons licence, and indicate if you modified the licensed material. You do not have permission under this licence to share adapted material derived from this article or parts of it. The images or other third party material in this article are included in the article's Creative Commons licence, unless indicated otherwise in a credit line to the material. If material is not included in the article's Creative Commons licence and your intended use is not permitted by statutory regulation or exceeds the permitted use, you will need to obtain permission directly from the copyright holder. To view a copy of this licence, visit <http://creativecommons.org/licenses/by-nc-nd/4.0/>.

© The Author(s) 2025